Photodissociation of HCN and HNC isomers in the 7-10 eV energy range

Aurelie Chenel, Octavio Roncero' , Alfredo Aguado, Marcelino Agúndez, and José Cernicharo

Photodissociation of HCN and HNC isomers in the 7-10 eV energy range

Aurelie Chenel,[1] Octavio Roncero,[1,a)] Alfredo Aguado,[2] Marcelino Agúndez,[3] and José Cernicharo[3]

[1]*Instituto de Física Fundamental (IFF-CSIC), C.S.I.C., Serrano 123, 28006 Madrid, Spain*
[2]*Departamento de Química Física Aplicada (UAM), Unidad Asociada a IFF-CSIC, Facultad de Ciencias Módulo 14, Universidad Autónoma de Madrid, 28049 Madrid, Spain*
[3]*Instituto de Ciencia de Materiales de Madrid, CSIC, C/ Sor Juana Inés de la Cruz 3, 28049 Cantoblanco, Spain*

The ultraviolet photoabsorption spectra of the HCN and HNC isomers have been simulated in the 7-10 eV photon energy range. For this purpose, the three-dimensional adiabatic potential energy surfaces of the 7 lowest electronic states, and the corresponding transition dipole moments, have been calculated, at multireference configuration interaction level. The spectra are calculated with a quantum wave packet method on these adiabatic potential energy surfaces. The spectra for the 3 lower excited states, the dissociative electronic states, correspond essentially to predissociation peaks, most of them through tunneling on the same adiabatic state. The 3 higher electronic states are bound, hereafter electronic bound states, and their spectra consist of delta lines, in the adiabatic approximation. The radiative lifetime towards the ground electronic states of these bound states has been calculated, being longer than 10 ns in all cases, much longer that the characteristic predissociation lifetimes. The spectra of HCN is compared with the available experimental and previous theoretical simulations, while in the case of HNC there are no previous studies to our knowledge. The spectrum for HNC is considerably more intense than that of HCN in the 7-10 eV photon energy range, which points to a higher photodissociation rate for HNC, compared to HCN, in astrophysical environments illuminated by ultraviolet radiation. © *2016 AIP Publishing LLC.* [http://dx.doi.org/10.1063/1.4945389]

I. INTRODUCTION

HCN is one of the most abundant polyatomic molecules in interstellar and circumstellar media.[1,2] This molecule has two linear isomers, HCN and HNC, the latter being ≈0.6 eV above in energy than the former, with a barrier between them of ≈2 eV. The rovibrational levels of the two isomers have been measured with diverse experimental techniques,[3–9] and the isomerization process has been the subject of numerous theoretical studies.[10–16] The two isomers have been observed in many diverse astrophysical environments, such as diffuse and translucent interstellar clouds,[17,18] dense interstellar clouds,[19–21] star forming regions,[22–24] protoplanetary disks,[25] circumstellar envelopes around evolved stars,[26,27] the circumnuclear disk of the Galactic center,[28] external galaxies,[29–31] as well as in comets[32] and atmospheres of planets,[33] showing that HCN and HNC are ubiquitous in space.

The HCN/HNC abundance ratio shows important changes between different astrophysical environments. For example, in dense interstellar clouds, where the gas is largely shielded against external ultraviolet radiation, the HCN/HNC abundance ratio is ≈1,[34] while in regions illuminated by ultraviolet photons, HCN becomes more abundant than HNC, by a factor of ≈5 in both diffuse interstellar clouds[17] and in photon-dominated regions such as the Orion Bar.[35,36] Apart from the influence of ultraviolet radiation, the HCN/HNC abundance ratio does also show a marked dependence with temperature. In the coldest regions, both isomers have similar abundances, but as the cloud temperature increases, the HCN/HNC ratio becomes higher, reaching values up to ≈80 in hot cores such as Orion-KL.[22,23] To understand the underlying causes of these variations, it is of paramount importance to determine the rates of all processes of formation, excitation, and destruction of the two isomers. The rates of many reactive collisional processes involving HCN and HNC have been revisited recently,[37] and the rates of rotational excitation through inelastic collisions with H_2 and He have been also investigated.[34,38,39] The photodissociation, however, has been only studied for HCN (see below) but not for the HNC isomer. Photoprocesses are likely to regulate to a large extent the HCN/HNC abundance ratio in those interstellar regions exposed to an intense ultraviolet radiation field, where HCN is found to be more abundant than HNC. In particular, the destruction of both isomers in such regions is dominated by photodissociation rather than by chemical reactions with radicals or ions. The aim of this work is to present a comparative study of the photoabsorption cross section of the two isomers HCN and HNC in order to provide their photo-stability in astrophysical regions exposed to ultraviolet radiation.

There are several experimental works on individual electronic bands of the most stable isomer HCN. Herzberg and Hines[40] studied the weak absorption bands associated to the $1^1A''$ and $2^1A'$ electronic states. These bands are formed by narrow peaks, decaying by either electronic predissociation

a)Electronic address: octavio.roncero@csic.es

to the ground state or through tunneling across potential barriers due to avoided crossing with higher electronic states. These processes have been studied in detail by either experimental techniques[40–44] or theoretical simulations.[45–49] The band associated to the $3^1A'$ state was measured by Mcpherson and Simons[50] and the peaks were assigned.[50–52] Also, the photodissociation cross section of HCN has been studied experimentally over a wide wavelength interval, from 90 to 150 nm, by several authors.[53–55] However, in none of these publications, the photodissociation of the HNC isomer was studied.

The aim of this work is to provide a comparative study of the photoabsorption cross section of the two isomers HCN and HNC over a wide range of photon energy. For this purpose, the potential energy surface (PES) of the 7 lowest electronic states (4 of $^1A'$ and 3 of $^1A''$ symmetries) has been calculated. On these adiabatic PESs, the photoabsorption cross section is calculated using a quantum wave packet approach for the two isomers. The results have been compared with those from previous works when possible. For the 3 electronic bound states, 4 $^1A'$ and 2,3 $^1A''$, we have calculated the adiabatic rovibrational bound levels and their radiative lifetimes.

This work is organized as follows. In Section II, the *ab initio* methods and results obtained for the lowest 7 electronic states are presented. In Section III, a short description of the methods used to calculate the rovibrational states and photodissociation dynamics is presented, while the results obtained are shown and discussed in Section IV. Finally, some conclusions are extracted in Section V.

II. POTENTIAL ENERGY SURFACES

The PESs for the ground and excited electronic states of the HCN/HNC system were obtained with the internally contracted multireference configuration interaction (icMRCI) method which employs wave functions that explicitly depend on the electron-electron distance (icMRCI-F12),[56] as implemented in the MOLPRO suite of programs.[57] This method has been proved to be efficient for achieving near complete basis set limit correlation energies,[58] even with small basis sets. In these calculations, the correlation consistent F12 triple zeta basis sets,[59] VTZ-F12, have been used.

The reference configurations for the icMRCI-F12 are obtained from a full valence state-averaged complete active space MCSCF calculation (SA-CASSCF) with the frozen core approximation. The $1s$ orbitals of C and N are doubly occupied in the SA-CASSCF references and not correlated in the icMRCI calculations. The SA-CASSCF wave functions are optimized in the C_s point group, including 8 states of symmetry $^1A'$ and 6 states of symmetry $^1A''$. This selection allows to describe the degenerate electronic states that appear at linear geometries, HCN and HNC, corresponding to Π or Δ states in $C_{\infty v}$.

Finally, icMRCI-F12 calculations were done for four states of symmetry $^1A'$ and three of symmetry $^1A''$, including single and double excitations from the configuration state functions obtained in the SA-CASSCF calculations. With these state selections, the icMRCI-F12 calculations involve a number of contracted (uncontracted) configurations of the

order of 2.6×10^6 (42×10^6) for $^1A'$ states and 2.1×10^6 (40×10^6) for $^1A''$ states.

To obtain 3D PESs for the HCN/HNC system, *ab initio* calculations have been performed over a large grid in Jacobi coordinates (**r**, **R**), **r** being the CN vector and **R** the vector joining the CN center-of-mass (we have used the masses of the ^{12}C and ^{14}N) and the H. The Jacobi angle γ is defined by the scalar product $r R \cos(\gamma) = \mathbf{r} \cdot \mathbf{R}$. With this selection, $\gamma = 0$ corresponds to linear C–N–H (HNC isomer) and $\gamma = \pi$ to linear H–C–N (HCN isomer). The (r, R, γ) grid of 15 504 points used is defined as

$$r = 0.5, 0.9, 0.95, 1.0, 1.05, 1.10, 1.153, 1.2, 1.3, 1.4, 1.5,$$
$$1.6, 1.8, 2.1, 2.5, \text{ and } 3.0 \, a_0 \quad (16 \text{ values}),$$
$$R = 0.00 - 5.00 \, a_0 \qquad\qquad (51 \text{ values}),$$
$$\gamma = 0 - \pi \qquad\qquad\qquad\qquad (19 \text{ values}).$$

Using this grid, the *ab initio* icMRCI-F12 energies for the seven singlet electronic states have been fitted using 3D cubic splines, using the DB3INK/DB3VAL subroutines based on the method of de Boor[60] and distributed by GAMS.[61] Sathyamurthy and Raff[62] investigated the use of 1D, 2D, and 3D splines fit of *ab initio* data, presenting the first full 3D cubic splines fit to a triatomic surface. These authors studied the adequacy of a 3D cubic spline PES in quasiclassical trajectory studies and found that average magnitudes, like total reaction cross sections or energy partitioning distributions, were in good agreement with those obtained with the full analytic PES used as benchmark.

To analyze the accuracy of the cubic splines, we have performed several tests with less *ab initio* geometries, using the non-fitted points to estimate the root-mean-square (rms) error. Using about 2800-3100 non-fitted geometries with an energy lower than 12 eV (taking the zero of energy in the HCN minima of the ground electronic state $X^1\Sigma^+$), we have obtained an estimated rms error of 0.022, 0.029, 0.040, and 0.027 eV for the X^2A', $2^2A'$, $3^2A'$, and $1^2A''$ electronic states, respectively. Higher excited electronic states have many avoided crossings and, as a consequence, the estimated rms error grows up to 0.058-0.074 eV.

The transition dipole moments between the ground and excited electronic states have been described using 3D cubic splines. The sign of the transition dipole moments depends on the relative phase of the two electronic wave functions involved. To obtain continuous transition dipole moments, we have corrected the relative sign of the eigenstates among successive points along the γ coordinate, calculating the overlap of the wave functions in two grid points and imposing the diagonal matrix elements of the overlap matrix to be positive. The transition dipole moments vary a lot with the internal coordinates and present sudden changes in the regions of avoided crossings and conical intersections, as shown in Fig. 2. This introduces an extra difficulty in the interpolation. We have estimated the rms error using 900 extra points, not included in the interpolation, and have found an error of $\approx 0.09 \, ea_0$. In any case, it should be noted that the photodissociation cross section is only affected by the value of the transition moments in the regions covered by the bound eigenfunctions on the X electronic state. Several interpolation

and fitting schemes have been checked, all resulting in rather similar absorption spectra.

A. Topology of the PES

Schwenzer *et al.* studied low lying electronic states of HCN[63] and HNC,[64] using configuration interaction that includes all single excitations with respect to a single configuration selected to describe each electronic state. With this approach, they obtained the geometry and electronic excitation energies T_e for both isomers. Peric *et al.*[65] obtained the PESs of the valence-type singlet electronic states of HCN, using Multireference Single and Double excitation Configuration Interaction (MRDCI) approach. Later on, they used these PESs to study the vibrational structure of the electronic transitions $1^1\Sigma^- \leftarrow X^1\Sigma^+$, $1^1\Delta \leftarrow X^1\Sigma^+$, and $1^1\Pi \leftarrow X^1\Sigma^+$.[45,52] More recently, Xu *et al.*[46–48] obtained the PES for the $1^1A''$ and $2^1A'$ states and used them to study the predissociation dynamics of HCN and DCN. These PESs do not include the region of the hydrogen isocyanide HNC.

The main electronic configurations of the four $^1A'$ and three $^1A''$ electronic states are shown in Table I. The states $2,3^1A'$ and $1^1A''$ are dissociative electronic states whose main electronic configuration corresponds to the excited electron on a $7a'$ orbital. The states $4^1A'$ and $2,3^1A''$ are electronic bound states corresponding to excitations to the $8a'$, $2a''$, or higher molecular orbitals. These results are in agreement with those reported by Schwenzer *et al.*[63,64] and Nayak *et al.*[66] The electronic excitation energies T_0 of HCN are also compared in Table I with experimental results,[67] showing a good agreement. Because we are interested in study the correlation with the linear conformations, we have included the $C_{\infty v}$ symmetry for both isomers, HCN and HNC. The minimum of the ground electronic state, $X^1\Sigma^+$, corresponds to the HCN linear conformation ($\gamma = \pi$), and has an electronic configuration $\cdots 5a'^2 6a'^2 1a''^2 \equiv \cdots 5\sigma^2 1\pi^4$. In the HNC isomer ($\gamma = 0$), the electronic configuration is $\cdots 5a'^2 6a'^2 1a''^2 \equiv \cdots 1\pi^4 5\sigma^2$.

Therefore, the symmetry of the orbital $6a'$ changes from π in HCN to σ in HNC (while the orbital $5a'$ experiences the opposite behavior), as illustrated in Fig. 1, and their energies also cross. This behaviour explains the change in the electronic configuration from HCN to HNC and the transition dipole moments involving the ground electronic state, as explained below. On the contrary, the orbitals $7a'$ and $2a''$ keep the same character for HCN and HNC, as can be seen in Fig. 1. In these two orbitals, of π character at linear geometries, the $1s$ orbital of H cannot contribute. The situation changes at bent geometries, where symmetry restrictions disappear for the a' orbitals, and the $1s$ orbital of H has a notorious contribution. As a consequence, the states with a dominant configuration including the $7a'$ orbital have negative charge on the H atom, while for the others this charge is positive, as calculated with Mulliken population analysis. This difference in the electronic population on H produces a change of sign in the permanent electric dipole of the different electronic states.

The changes of the molecular orbitals produce a complex structure of crossings of electronic states, as shown in Fig. 2 as a function of the angle γ. It can be seen that the projection of the electronic orbital angular momentum Λ changes from HCN to HNC. For example, for HCN the third state has a Δ symmetry, while this is not the case for HNC. This is due to a sequence of avoided crossings clearly seen in the $0° < \gamma < 20°$ interval. This has important implications because $\Sigma^+ \rightarrow \Sigma^-, \Delta$ transitions are electric dipole forbidden. Thus, for the HCN isomer, the $1^1A''$ electronic state, which correlates to the $^1\Sigma^-$ state, and the $2^1A'$ and $2^1A''$ electronic states, correlating to the $^1\Delta$ state, show a very small electric dipole transition moments from the ground electronic state, while for HNC this is not the case. This change of symmetry from HCN to HNC is a consequence of the orbital crossing between the 1π and 5σ orbitals. For example, the first excited state $1^1A''$ ($\cdots 1a'' 7a'$) correlates with the $1^1\Sigma^-$ electronic state of HCN ($\cdots 5\sigma^2 1\pi^3 2\pi$) and with the $1^1\Pi$ electronic state of HNC ($\cdots 1\pi^4 5\sigma 2\pi$).

TABLE I. Electronic excitation energies and correlation of the PES with the linear HCN and HNC isomers.

	State			T_e (eV)	T_0 (eV)		T_e (eV)
C_s	HCN	HNC	Main configurations[a]	HCN	Calc.	Expt.[b]	HNC(Calc.)
$1^1A'$	$X^1\Sigma^+$	$X^1\Sigma^+$	$\cdots 5a'^2 6a'^2 1a''^2$	0	(0.430)[c]	$\ldots$	(0.323)[d]
$2^1A'$	$1^1\Delta$	$2^1\Sigma^+$	$\cdots 5a'^2 6a'\ 1a''^2 7a'$	7.04	6.88	6.77	6.47
			$\cdots 5a'\ 6a'^2 1a''^2 7a'$				
			$\cdots 5a'^2 6a'^2 1a''\ 2a''$				
$3^1A'$	$1^1\Pi$	$1^1\Pi$	$\cdots 5a'^2 6a'\ 1a''^2 7a'$	8.29	8.16	8.14	7.94
			$\cdots 5a'\ 6a'^2 1a''^2 7a'$				
			$\cdots 5a'^2 6a'^2 1a''\ 2a''$				
$4^1A'$	$2^1\Pi$	$2^1\Pi$	$\cdots 5a'^2 6a'\ 1a''^2 8a'$	9.36			
$1^1A''$	$1^1\Sigma^-$	$1^1\Pi$	$\cdots 5a'^2 6a'^2 1a''\ 7a'$	6.56	6.41	6.48	6.19
$2^1A''$	$1^1\Delta$	$2^1\Pi$	$\cdots 5a'^2 6a'\ 1a''^2 2a''$	7.81	7.70		7.48
			$\cdots 5a'^2 6a'^2 1a''\ 7a'$				
$3^1A''$	$1^1\Pi$	$3^1\Pi$	$\cdots 5a'\ 6a'^2 1a''^2 2a''$	9.05	9.01	8.88	8.25

[a] $\cdots$ refers to doubly occupied orbitals $1a'^2 2a'^2 3a'^2 4a'^2$.
[b] Experimental values taken from Ref. 67.
[c] Zero point energy from Ref. 15.
[d] Zero point energy from Ref. 15, taken from the minimum of the HNC isomer, 0.657 eV over the HCN minimum.
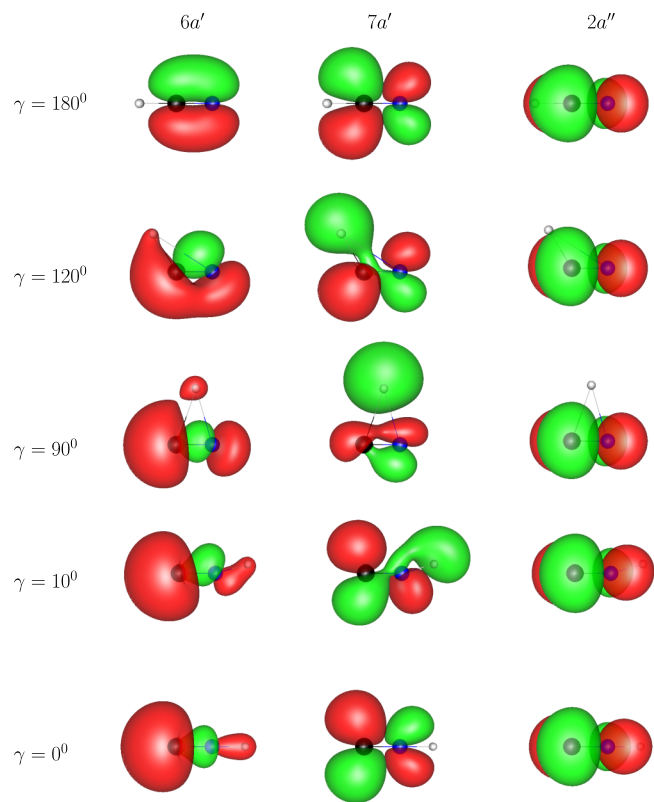
FIG. 1. Molecular orbitals of HCN at $r = 1.153$ Å and $R = 1.7$ Å for different angles, γ.

FIG. 2. Angular dependence of the potential of the lowest electronic states of HCN for $r = 1.153$ Å and $R = 1.7$ Å (bottom panel) and of the transition electric dipole moments between the ground and some excited electronic states (top panel). The symmetry at the two linear geometries is also shown.

The HCN/HNC PES for several electronic states of $^1A'$ and $^1A''$ symmetry is shown in Fig. 3 as a function of R for $r = 1.153$ Å (HCN in the left panel and HNC in the right panel). The middle panel shows the electronic states of CN as a function of CN internuclear distance, r, which in the other two panels was fixed at the equilibrium distance of CN in the ground electronic state of HCN($X^1\Sigma^+$). The ground state $1^1A'$ correlates to CN($X^2\Sigma^+$) + H(^2S) and is deeply bound, by ≈ 5.5 eV, presenting the deepest well for the HCN isomer.

The first two excited electronic states, $2^1A'$ and $1^1A''$, correlate with the first excited state CN($A^2\Pi$) + H(^2S). These two states are essentially dissociative down to distances of $R \approx 1.5$ Å, where they cross with other excited states correlating to excited states of CN, $D^2\Pi$, or higher. This avoided crossing originates a barrier with a local well, whose minimum is higher than the dissociation energy. The crossing depends on the angle γ leading to different well depths for the HCN and HNC isomers. The $3^1A'$ state correlates to CN($B^2\Sigma^+$) + H(^2S) and is repulsive for HCN and attractive for HNC, leading to avoided crossings with the higher electronic states at rather different distances. These avoided crossings give rise to a rather deep well in the HNC isomer but not for HCN. Higher electronic states correlate with excited electronic states of CN, leading to a dissociation threshold above 12 eV over the minimum of the HCN(X^1A') state. These states present deep wells for both HCN and HNC isomers.

The wells of the different electronic states are clearly seen in Fig. 4, where the contour plots of the lowest 7 potential energy surfaces calculated here are shown as a function of $X = R\cos\gamma$ and $Y = R\sin\gamma$. The C and N atoms are placed
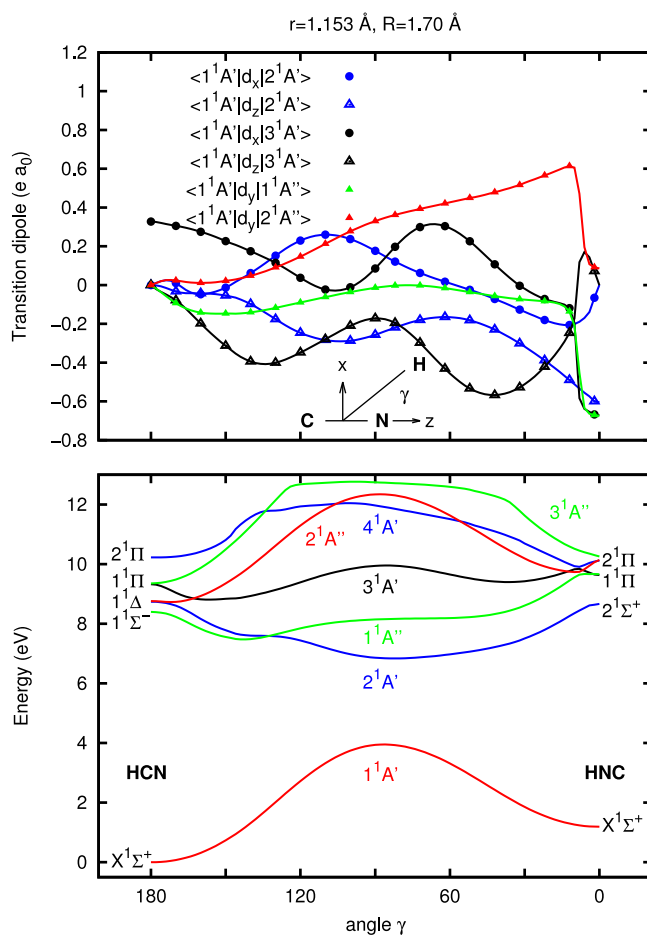
in the X axis ($Y = 0$) at $X = -0.621$ Å and $X = 0.532$ Å, respectively.

There are many avoided crossings among the adiabatic states, as shown in Fig. 3. At these crossings, non-adiabatic couplings are expected to play an important role in the
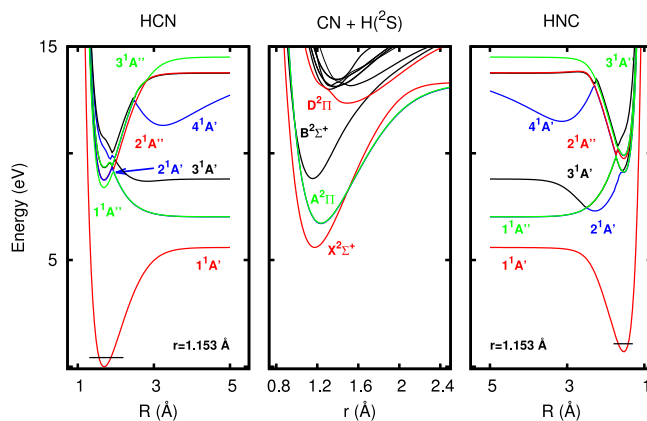

FIG. 3. Potential energy cuts of isolated CN as a function of internuclear distance r (central panel) and of linear HCN (left panel) and HNC (right panel) as a function of the distance R between H and the center-of-mass of CN (kept frozen at $r = 1.153$ Å).
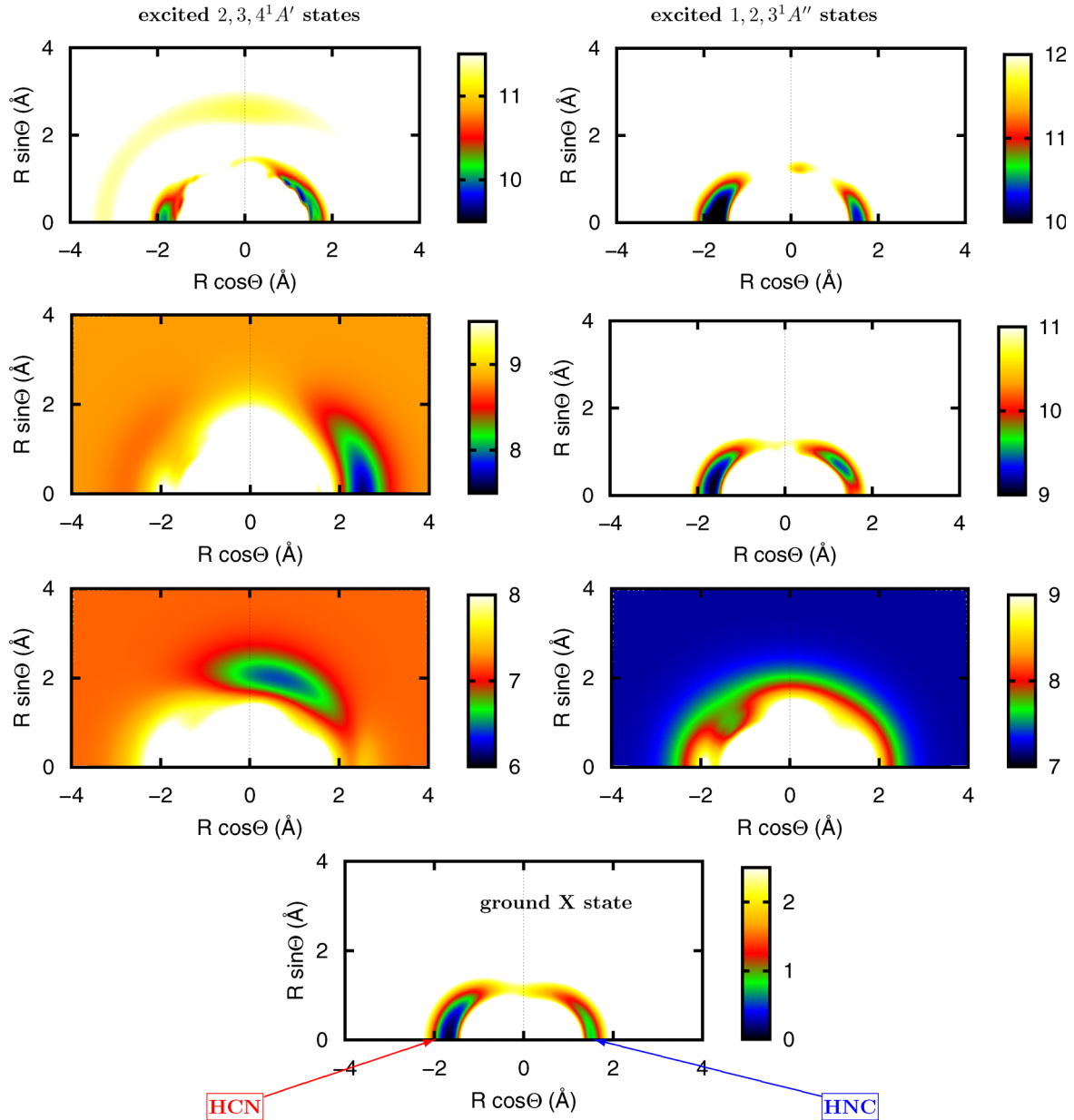
FIG. 4. Contour plots of the potential energy surfaces calculated in this work as a function of $R\cos\gamma$ and $R\sin\gamma$, for a fixed CN internuclear distance of $r = 1.153$ Å. Energies (in eV) are referred to the minimum of the HCN well of the ground state.

photodissociation dynamics, although these couplings are neglected in the present study. These effects can be classified as bound-bound interaction, producing a shift and broadening of peaks, and bound-free transitions, producing the dissociation of adiabatically bound levels, and hence the broadening. These two aspects are further discussed below when discussing the dynamical results.

III. DYNAMICAL METHODS

The dynamical calculations have been performed in Jacobi coordinates, as described above. A body-fixed frame, defined by three Euler angles (ϕ, θ, χ), is used in which the three atoms are in the x-z plane, with the z-axis being parallel to **R**, and $r_x = r\sin\gamma$ being positive. Thus the wave functions are expressed as

$$\Psi_k^{J\lambda M\epsilon}(\mathbf{r},\mathbf{R}) = \sum_\Omega \frac{\Phi_k^{J\epsilon\lambda\Omega}(r,R,\gamma)}{rR} W_{M\Omega}^{J\epsilon}(\phi,\theta,\chi)|\lambda\rangle, \quad (1)$$

where J is the quantum number associated to the angular momentum operator **J**, with projections M and Ω on the space-fixed and body-fixed z-axis, respectively, and $|\lambda\rangle$ is the adiabatic electronic wave function. $\epsilon = \pm 1$ is the parity under spatial inversion of coordinates. The number k denotes all the required quantum numbers to characterize a state. Finally

$$W_{M\Omega}^{J\epsilon}(\phi,\theta,\chi) = \sqrt{\frac{2J+1}{16\pi^2(1+\delta_{\Omega,0})}}$$
$$\times \left[D_{M,\Omega}^{J*}(\phi,\theta,\chi) + \epsilon(-1)^{J+\Omega} D_{M,-\Omega}^{J*}(\phi,\theta,\chi) \right]$$
$$(2)$$

are parity adapted functions, with $D^J_{M,\Omega}$ being Wigner rotation matrices[68] corresponding to a total angular momentum J. The $\Phi^{J\epsilon\lambda\Omega}_k(r,R,\gamma)$ coefficients are represented in grids: for the radial variables, they consist of equi-spaced points, while for γ a Gauss-Legendre quadrature is used. These coefficients are calculated numerically with the program MADWAVE3[69,70] as implemented for photo-initiated processes, for infrared,[71] electronic,[72] and photodetachment[73] processes in one or several electronic states. Here we only present some details of the calculations, regarding bound states and time propagation calculations.

A. Bound states

The bound states are calculated in the mixed grid/basis representation using a non-orthogonal iterative Lanczos procedure[74] in two steps. The eigenvalues E^λ_k are first obtained with a non-orthogonal Lanczos procedure following the method of Cullum and Willoughby.[75] The eigenstates are then obtained iteratively using the conjugate gradient method.[76,77] The grid is formed by 64 and 256 equally spaced points in r and R, respectively, in the intervals $0.5 \le r \le 3$ Å and $0.001 \le R \le 6$ Å. A Gauss-Legendre quadrature is chosen for the angle γ formed by 200 points. Most of the calculations presented below are restricted to $J = 0$ and $J = 1$. Also, the calculations are performed on a single adiabatic electronic state $|\lambda\rangle$.

The use of a grid facilitates the calculation of very excited states. The action of the Hamiltonian on this grid

representation is performed using sine Fourier transforms for the radial derivatives, and the angular kinetic operator is evaluated as described previously,[78] as implemented in the MADWAVE3 code described elsewhere.[69,70]

B. Wave packet calculations

In a first order perturbative treatment, the total absorption cross section for electric dipole transitions from an initial state k, in the electronic state $|\lambda_i\rangle$ and with angular momentum J_i, to an excited electronic state $|\lambda\rangle$ with total angular momentum J, is given by

$$\sigma(h\nu) = Ah\nu \sum_{M_i} \frac{1}{2J_i + 1} \times \sum_\alpha \left| \left\langle \Psi^{J\lambda M\epsilon}_{E\alpha} |\mathbf{d}\cdot\mathbf{e}| \Psi^{J_i\lambda_i M_i\epsilon_i}_k \right\rangle \right|^2, \tag{3}$$

where $E = E^{\lambda_i}_k + h\nu$, $A = 1/\hbar^2\epsilon_o c$, $\mathbf{d}$ is the electric dipole of the molecule, $\mathbf{e}$ is an unitary vector parallel to the electric field of the radiation, and $\Psi^{J\lambda M\epsilon}_{E\alpha}$ is a dissociative wave function of energy E leading to H + CN fragments, with CN in the rovibrational level $\alpha \equiv v,j$ and electronic state correlating to the state λ of HCN. Within a time-dependent framework, this expression transforms to

$$\sigma(h\nu) = \frac{Ah\nu}{2\pi\hbar}\frac{2J+1}{3}\int dt\, e^{iEt/\hbar} \left\langle \Psi^{J\lambda\epsilon}_{t=0}|\Psi^{J\lambda\epsilon}_t \right\rangle, \tag{4}$$

where linear polarization of the radiation has been assumed. The components of the initial wave packet in Eq. (1) are given by Refs. 71 and 72,

$$\Phi^{J\epsilon\lambda\Omega}_{t=0}(r,R,\gamma) = \sum_{q\Omega_i} \Phi^{J_i\epsilon_i\lambda_i\Omega_i}_k(r,R,\gamma)d^{\lambda\lambda_i}_q(r,R,\gamma)\frac{(-1)^{q-\Omega_i}\ (1 - \epsilon\epsilon_i)}{2\sqrt{(1+\delta_{\Omega0})(1+\delta_{\Omega_i0})}} \left\{ \begin{pmatrix} J & 1 & J_i \\ \Omega & -q & -\Omega_i \end{pmatrix} + \epsilon_i(-1)^{J_i} \begin{pmatrix} J & 1 & J_i \\ \Omega & -q & \Omega_i \end{pmatrix} \right\}, \tag{5}$$

where $d^{\lambda\lambda_i}_q(r,R,\gamma)$ is the electric transition dipole moment matrix elements between the electronic states $|\lambda_i\rangle$ and $|\lambda\rangle$.

The wave packet is propagated with a modified Chebyshev integrator.[69,79–84] The grid used is that used for the bound state calculations described above, except in the number of points in the grid of R, which is duplicated using the same radial intervals. The wave packet is absorbed in the interval 5 Å $< R <$ 12 Å, with the function $\exp[-0.0001(R-5)^4]$, to avoid reflexions when the wave packet reaches the edges of the grid. For dissociative electronic states, the propagation is performed during 50 000 Chebyshev iterations, while for bound electronic states, the propagation is continued until 100 000 iterations. The autocorrelation function in Eq. (4) is multiplied by an exponential function $e^{-2\Gamma t}$, leading to a Lorentzian broadening for the narrow lines in the spectra, with a width of $\Gamma \approx 0.5$ meV in the present case.

The narrow resonances can be assigned from the analysis of the wave function at the energy of the peak using a pseudo-spectral method,[71,85,86] which in the case of using a modified Chebyshev propagator is implemented in Refs. 69 and 87.

C. Radiative lifetimes

The excited electronic bound states present deep wells, with bound or quasi-bound states. Without considering non-adiabatic transitions, these states can only disappear by non-stimulated emission towards lower electronic states. The radiative lifetime of these states is given by the inverse of the Einstein coefficients, which are calculated in a first-order perturbative treatment as

$$A^{J\lambda\epsilon k} = \sum_{MM_f}\sum_{J_f\lambda_f\epsilon_f k_f} \frac{1}{3\pi\epsilon_0\hbar^4}\left(\frac{h\nu}{c}\right)^3$$

$$\times \left| \left\langle \Psi^{J_f\lambda_f M_f\epsilon_f}_{k_f} |\mathbf{d}\cdot\mathbf{e}| \Psi^{J\lambda M\epsilon}_k \right\rangle \right|^2. \tag{6}$$

Here we only consider transitions from excited electronic states to the ground state, between $J = 0$ and $J_f = 1$. In addition, we classify the final levels on the ground electronic state as corresponding to either HCN or to the HNC isomer. Thus, it is possible to study the process of photoisomerization, i.e., isomerization after electronic excitation and subsequent emission.

IV. DYNAMICAL RESULTS AND DISCUSSION

A. Vibrational levels on the ground state

There are several previous PESs calculated for the ground electronic state of HCN.[13,15,88,89] This state has a double minimum at collinear geometries, corresponding to the HCN and HNC isomers, and its spectroscopy has been widely studied theoretically.[13–15] The shape of this potential has been also studied with a valence-bond curve crossing model, and the angular dependence explained as the result of avoided-crossings among the three lower diabatic curves.[90]

The angular minimum energy path (MEP) from HCN to HNC along the ground PES obtained in this work is compared in Fig. 5 to those obtained using the two most recent PESs of van Mourki *et al.*[13] (hereafter VQZANO+ PES) and Varandas and Rodrigues[15] (hereafter VR PES). The three MEPs show a similar behavior. The present PES has a barrier height slightly lower than the VR PES, and in both of them the height is lower than in the VQZANO+ PES. The HNC minimum energy in the VQZANO+ and VR PESs are very close, and in both, it is slightly lower than in the present PES.

We have calculated the bound states using the three PESs. The energies and assignment of the bound states obtained with the VQZANO+ and VR PESs are essentially equal to those reported by those authors,[13,15] with differences of tenths of wavenumbers or less for the first levels. The results obtained with the present PES are slightly different. The energy of the lowest bound state of HCN is 0.4306, 0.4316, and 0.4239 eV using the VR, VQZANO+, and the present PES, respectively. For HNC, the energy of the first level with respect to the zero of energy corresponding to the equilibrium geometry of HCN is 1.0749, 1.0746, and 1.0845 eV for the VR, VQZANO+, and the present PES, respectively.
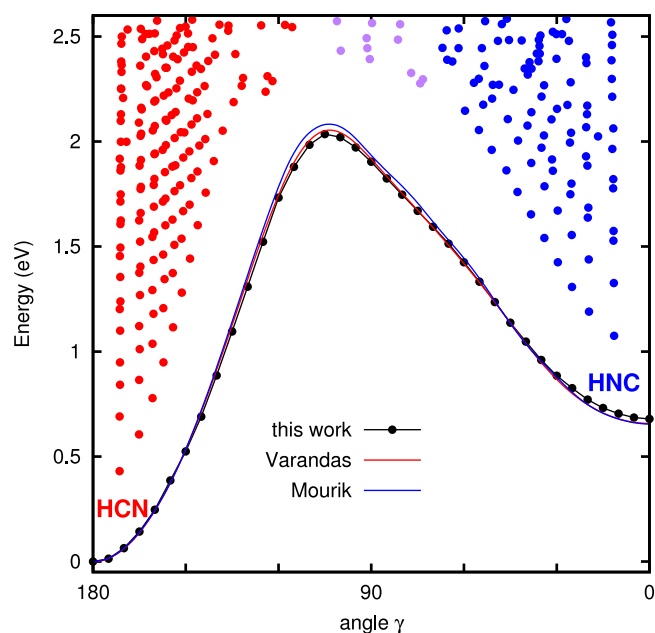

FIG. 5. Minimum energy path for the HCN/HNC isomerization in the HCN (X) PES of the present work, compared with those obtained from the PES of Refs. 13 and 15. The points correspond to the 270 energy levels calculated with the VR PES[15] for $J = 0$, and the angle corresponds to the average of γ of each vibrational state.

The present results are slightly different from the previous ones. The differences arise from the *ab initio* calculation. In the present work, we have calculated several electronic states, optimizing the molecular orbitals with a CASSCF procedure for an average of all them together. This generates a very large active space and it is necessary to reduce it by using a frozen core approximation. For this reason, hereafter we shall consider the bound states on the VR PES, which is considered to be the most accurate one.

In Fig. 5, we also show the energies of the first 270 vibrational levels as a function of the average value $\langle\gamma\rangle$, calculated with the VR PES. For energies below ≈ 2.3 eV, the average value of the angle γ remains in either the HCN or the HNC wells, and varies with the bending excitation of the state. The bound states can be assigned to each isomer even above the isomerization barrier, of ≈ 2.1 eV, because of the zero-point energy. Above 2.4 eV, the bound states start to be located on both wells but there are still some of them being associated to one of the two isomers. Note that $\langle\gamma\rangle$ can be used to assign the bound state to either one or other isomer.

B. Photoabsorption of the electronic dissociative states

The photodissociation spectra from the HCN ($k = 1$, at E = 0.43 eV) and HNC ($k = 11$, at E = 1.07 eV) vibrational states on the ground HCN (X^1A') state towards each of the 6 excited electronic states are shown in Fig. 6, for the $J_i = 0 \rightarrow J = 1$ rotational transition.

The arrow in each panel indicates the dissociation threshold on each electronic state and allows to classify the spectra into three groups, according to the Franck-Condon region where the initial wave packet lies (see Fig. 4). For the $2^1A'$ and $1^1A''$ states, the absorption spectra are above the CN ($A^2\Pi$, $v = 0$, $j = 0$) + H (^2S) dissociation threshold (see Fig. 3). The spectrum corresponding to the $3^1A'$ state is formed by a broad envelope of narrow peaks associated to resonances (above the threshold) and bound states (below the threshold) within the Born-Oppenheimer approximation. Finally, the spectra associated to the $4^1A'$, $2^1A''$, and $3^1A''$ electronic bound states are well below their corresponding dissociation threshold and consist of delta functions associated to bound states, because non-adiabatic transitions are neglected in this work. These peaks are broadened by ≈ 0.5 meV, a value obtained by multiplying the autocorrelation function by a exponential function, as described above.

The main difference between the spectra of HCN and HNC is the intensity for the $2^1A'$, $1^1A''$, and $2^1A''$ states. In these three cases, the absorption cross section for the HCN isomer is nearly 2 orders of magnitude lower than for the HNC isomer (note that in Fig. 6 the corresponding spectra for HCN are multiplied by 50). This lower intensity is due to the symmetry of the electronic states at linear HCN and HNC geometries, leading to very different transition dipole moments. The $1^1A''$ state correlates to a $^1\Sigma^-$ state in the HCN linear configuration while it correlates to a $^1\Pi$ state in the HNC one (see Fig. 2). At collinear geometries, $\Sigma^+ \rightarrow \Sigma^-$ transitions are forbidden while $\Sigma^+ \rightarrow \Pi$ transitions are allowed, explaining why the spectrum of HCN ($1^1A''$) is
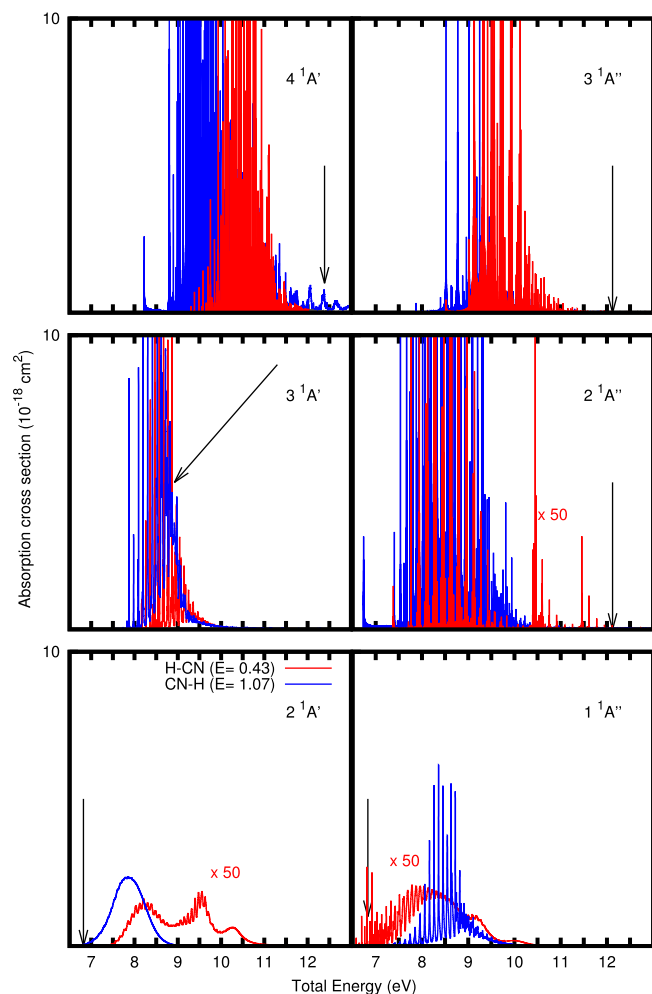
FIG. 6. Absorption spectrum for the $J_i = 0 \rightarrow J = 1$ transition from the ground electronic state to each of the 6 excited electronic states of HCN. Transitions from the first vibrational level of HCN and HNC isomers (vibrational levels $k = 1$ and 11, respectively) are shown in red and blue lines, respectively. The arrow indicates the dissociation energy leading to CN ($v = 0, j = 0$) fragments. The zero of energy is at the HCN equilibrium configuration of the ground electronic state.

FIG. 7. Absorption spectrum for the $J_i = 0 \rightarrow J = 1$ transition from the HCN isomer in the ground electronic state to the $1^1A''$ state of HCN (top panel) and HNC (bottom) isomers. Energy is referred to the CN (A$^2\Pi$, $v = 0, j = 0$) threshold, at E = 6.82 eV with respect to the equilibrium configuration of HCN on the ground electronic state. The contour plots of the wave functions at the energies of some of the resonances and $r = 1.2$ Å are shown in the middle panels. The distribution on r, R for each of the resonances is shown in the right panels, integrating over the angle γ.

less intense than that of HNC ($1^1A''$). Similar arguments hold for the $2^1A'$ state, which correlates to $^1\Delta$ and $^1\Sigma^+$ symmetries for the HCN and HNC isomers, and for the $2^1A''$ state, which correlates to $^1\Delta$ and $^1\Pi$ symmetries, as shown in Fig. 2.

The weak absorption bands between 200 nm and 160 nm for the HCN isomer were first assigned by Herzberg and Hines[40] to bending progressions in the $1^1A''$ state, due to a linear to bent transition. These bands correspond to predissociative peaks.[40–44] Below the CN (A$^2\Pi$, $v = 0$) + H (^2S) threshold, these resonances can only decay by non-adiabatic electronic predissociation and they are extremely narrow. Above this threshold, the predissociation is through a barrier and their widths are larger, depending on the nature of the resonance. These bands have been studied extensively, as reviewed in a series of works by Xu *et al.*[46–49]

The absorption spectrum associated to the $1^1A''$ state of the HCN isomer is shown in the top panel of Fig. 7 and can be compared with that in Fig. 4 of Ref. 47. The differences are attributed to differences in the PESs
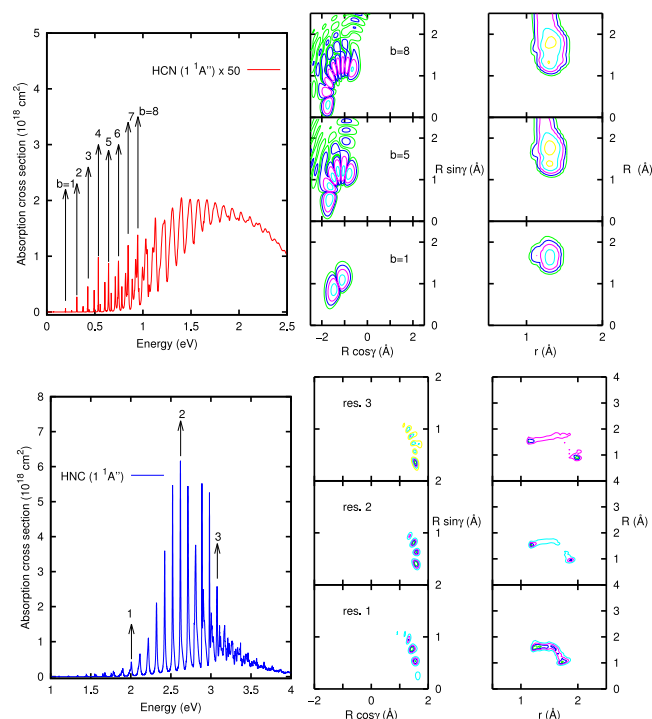
and in the transition electric dipole used. For example, Xu *et al.*[47] neglected the overall rotation and the $2^1A' \leftarrow 1^1A'$ transition was approximated by a simple sum of the x and y contributions. Also, here we use as zero of energy the CN (A$^2\Pi$, $v = 0$, $j = 0$) + H threshold, and the autocorrelation function is multiplied by a decaying exponential function, which introduces a broadening in the lower peaks, below 1 eV of kinetic energy, of approximately 0.5 meV. This broadening reduces the height of the narrowest peaks, and this effect depends on the real width of the levels, but the total integrated intensity along the whole absorption profile for each transition remains the same. The peaks above 1 eV are broader, indicating a fast predissociation rate. As a consequence, as energy increases, the wave function for the resonances has a larger continuum contribution, as can be observed in the right panels of Fig. 7 for large R values.

As previously suggested by other authors,[40–44,46–49] the peaks associated to the HCN ($1^1A''$) state are a bending progression on the HCN side. The peaks labeled with $b = 1, 5$ and 8 show the corresponding nodal structure in the middle-right panels of Fig. 7. Also, the distribution in r and R shows little excitation. For kinetic energies below 0.7 eV, the lower peaks also show a bending progression but with some excitation in r or R. As energy increases all motions start to mix, and that is why for $b = 5$ and 8 there is a small contribution from a vibrational quantum in R, as shown in the right panels of Fig. 7.

A similar analysis has been done for the HNC isomer on the same $1^1A''$ state in the bottom panels of Fig. 7. As commented above, this spectrum is much more intense and could be also assigned to a bending progression. However, the analysis of the wave function at the peaks demonstrate that they correspond to highly excited bending levels on the HNC side but they also show a wide distribution on r and R. In this case, the motions on the three internal coordinates are more mixed, making more difficult their assignment. Note that the angular distribution of the wave functions lies on the HNC side and does not coincide with the levels reached for the HCN isomer (see middle panels of Fig. 7). The potential of the $1^1A''$ state does not show a well for $r = 1.153$ Å in Fig. 4, although it does for longer r values.

The spectra of HCN and HNC on the $3^1A'$ state are both of similar intensity and consist of relatively narrow peaks, distributed below and above the CN $(B^2\Sigma^+, v = 0) + $ H (^2S) dissociation threshold. The spectrum of the HCN isomer has been measured by Mcpherson and Simons,[50] who assigned the peaks to bending and H-CN stretching. The spectrum simulated in this work for the HCN isomer is shown in the left top panel of Fig. 8, together with the plot of the probability associated to some selected resonances, in the right panels. In all cases, the nodal structure of the wave functions corresponds to the ground level of the CN vibration, and different excitation on γ and R coordinates, in good agreement with previous assignments.[50,51] Also, the position and spacing of the peaks approximately coincide with the experimental ones.

The peaks below the zero of energy correspond to dissociation by non-adiabatic transitions towards CN $(X^2\Sigma^+$ or $A^2\Pi) + $ H (^2S) states. Above the zero of energy, the width of the peaks increases considerably indicating a fast dissociation on the same adiabatic $3^1A'$ state, leading to CN $(B^2\Sigma^+)$ fragments. The width of the peaks varies depending on the nature of the associated vibrational mode, either bending or H-CN stretching, as found experimentally.[50] For example, the peak labeled $b = 4$ has a half width at half maximum of $\Gamma = 0.6$ meV, close to the artificial broadening introduced by multiplying the autocorrelation function by a decaying exponential function. This indicates that the predissociation rate is rather low. The peak labeled $b = 5$ is broader, with $\Gamma = 1.1$ meV, and the peak labeled with $b = *$, at 0.273 eV, has a width of $\Gamma = 1.3$ meV. All these states present a rather long lifetime because as bending excitation increases, predissociation slows down, as found previously.[50,51] The lower peaks of the spectrum in Fig. 8 correspond to H-CN stretching or to a combination of various modes and present broader widths.

The resonances reached from the excitation of HCN (X) to the $3^1A'$ state are supported by a small well that is shown in Fig. 4 for $R\cos\gamma < 0$, in the HCN side. There is a deeper well on the HNC side $(R\cos\gamma > 0)$ but is placed at longer R distances, $R > 2$ Å. For this reason, the spectrum of HNC associated to the $3^1A'$ state is shifted to higher energies, with all peaks being nearly above the CN $(B^2\Sigma^+, v = 0, j = 0) + $ H (^2S) threshold. Nevertheless, the peaks below 0.5 eV can be nicely associated to a bending progression. Above 0.5 eV, all the modes are more mixed and it becomes more difficult to separate the contribution from the continuum and thus to make the assignments.

These quasi-bound states can predissociate, and their widths increase with energy. Level $b = 1$, at 9.127 meV above the threshold, has a width of $\Gamma = 2.6$ meV, while for $b = 3$ the width is $\Gamma = 3.5$ meV. The peak labelled with $*$ is mixed with some other peaks and it is difficult to estimate its width, although it is broader than peaks lying at lower energies, indicating that as available energy increases, the width also increases.

The absorption spectra of HCN and HNC associated to the $3^1A'$ state (see Fig. 8) show a comparable intensity, and the bending progression have similar spacings, ≈ 0.095 eV and 0.109 eV for HCN and HNC, respectively. However, the resonances reached in the excitation of each isomer are different due to Franck-Condon arguments.

FIG. 8. Absorption spectrum for the $J_i = 0 \to J = 1$ transition from the HCN isomer in the ground electronic state to the $3^1A'$ state of HCN (top panel) and HNC (bottom) isomers. Energy is referred to the CN $(B^2\Sigma^+, v = 0, j = 0)$ threshold, at 8.93 eV with respect to the equilibrium configuration of HCN on the ground electronic state. The contour plots of the wave functions at the energies of some of the resonances and $r = 1.2$ Å are shown in the middle panels. The distribution on r, R for each of the resonances is shown in the right panels, integrating over the angle γ.

C. Photoabsorption to the electronic bound states

The absorption towards the $4^1A'$ and $2,3\ ^1A''$ electronic bound states is always below their adiabatic dissociation threshold, i.e., towards the bound states on each adiabatic surface. In all the cases, there are separate wells corresponding to the HCN and HNC isomers, but the MEPs, in Fig. 9, are in general more complex. For the $4^1A'$ state, there are many minima and maxima as a consequence of the high number
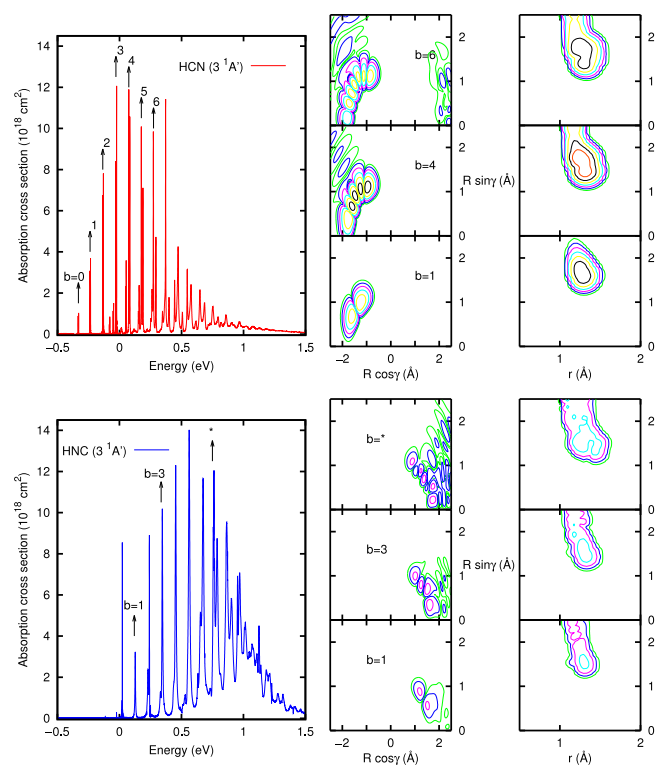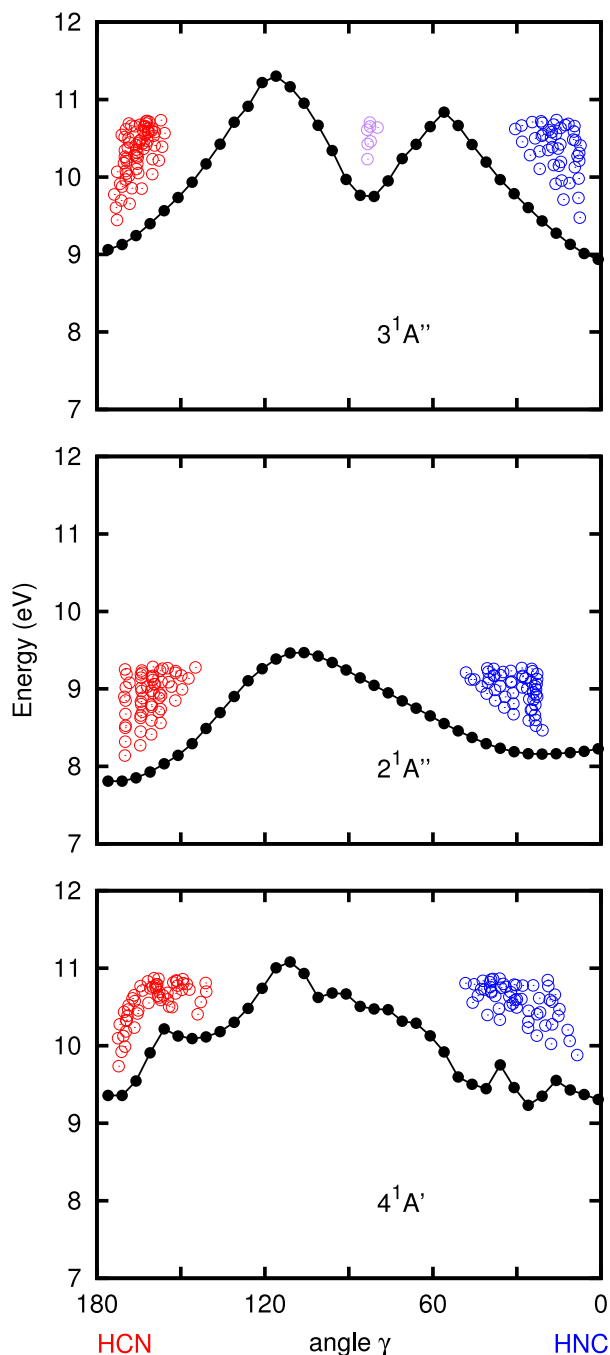
FIG. 9. Minimum energy path for the HCN/HNC isomerization for the $4^1A'$ and $2,3\,{}^1A''$ electronic bound states and first 100 bound states as a function of the angle $\langle\gamma\rangle$.

of curve crossing, and the two isomers have approximately the same well depth. The $2^1A''$ state presents a double well similar to that of the ground state, with HCN having the deepest one. However the energy difference between HCN and HNC isomers is smaller and the barrier is approximately a half. Finally, the $3^1A''$ state presents a third well for $\gamma \approx \pi/2$, less deep than the HCN and HNC wells, which have nearly the same energy.

The energies of the first 120 bound states are also shown in Fig. 9. As for the ground electronic state, these bound states are clearly localized in either the HCN or the HNC isomer, except for the $3^1A''$ where few states are located in the well

at $\gamma \approx \pi/2$. In all the cases, the energies of the bound states are not as regular as in the ground electronic state. The reason is that the vibrations are not so separable, presenting a more complex distribution of nodes. This makes more difficult the assignment of approximate quantum numbers.

This localized character of the bound states makes that absorption from a given isomer on the ground state reaches bound states on the excited state corresponding to the same isomer. These states should decay through non-adiabatic couplings towards the lower dissociative states to produce CN in X ($^2\Sigma^+$), A ($^2\Pi$) or/and B ($^2\Sigma^+$), currently under study. Alternatively, they could decay through non-stimulated emission towards lower states as described below.

D. Total absorption spectra

There are several experimental works on the HCN absorption spectrum over a broad wavelength interval, from 90 nm to 150 nm,[53–55] although there is no experimental spectrum for the HNC isomer. These spectra may differ between them due to the different experimental conditions employed, such as the temperature and the monochromator bandwidth as a function of the wavelength,[53] which may reduce the height of narrow peaks, specially those appearing at longer wavelengths. The simulated total spectrum of HCN is compared with the experimental one[55] in the bottom panel of Fig. 10.

For energies below 8.4 eV, the narrow peaks in the simulated spectrum are absent in the experimental one probably because they are much narrower than the experimental bandwidth.

In the 8.5-9 eV interval, the experimental and simulated peaks show similar progressions at the same energies, but the intensities are different. We have tried several fittings of the transition dipole moment for the $1^1A' \rightarrow 3^1A'$ transition, but the intensities obtained did not vary significantly. Since the simulated and experimental spectra agree with respect to the position of the peaks, it is expected that the adiabatic potential for the $3^1A'$ is essentially correct. The differences are attributed to non-adiabatic or Coriolis couplings to other states, which allow to share the oscillator strength and change the widths of the resonances, thus reducing the maximum height of individual peaks.

The series of narrow and intense peaks starting at 9.1 eV correspond to the $3^1A''$ state. In this case, the peaks are shifted with respect to the experimental ones. In this electronic state, the bound vibrational levels reached cannot decay in the adiabatic approximation. Their apparent widths in the spectrum is only the 0.5 meV introduced artificially as described above. This explains why the peaks are so narrow and intense. Another factor affecting the width of the experimental peaks is the average over several rotational transitions, due to the presence of several initial rotational states under thermal conditions. In this work, we only consider a single rotational transition, $J_i = 0 \rightarrow J = 1$, and thus the peaks in the simulated spectra are narrower. Several rotational transition will be considered in a future work.

The bound levels of the $3^1A''$ state can only decay by emitting photons or through the couplings to other dissociative
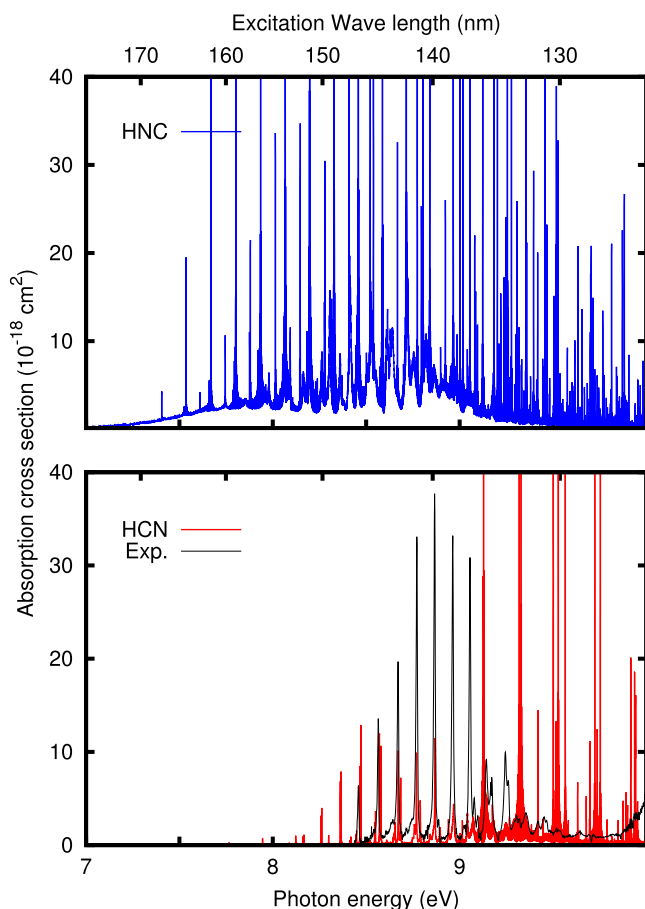
FIG. 10. Simulated spectrum versus experimental one, from Ref. 55, for HCN (bottom panel). Top panel shows the simulated spectrum for the HNC isomer.

electronic states. These couplings have been attributed to non-adiabatic, when belonging to the same symmetry, Coriolis couplings, between $^1A'$ and $^1A''$ states, or spin-orbit couplings, for different multiplicities. In any case, when considering these couplings, the levels would become broader and could share their oscillator strength with other close lying bound states.

For energies above 10 eV, there are higher Rydberg states which also contribute and must be included to describe that region of the spectrum. Also the couplings to other electronic states should be accounted for to properly describe the spectra. Work in these two directions is now being conducted.

The absorption spectrum of the HNC isomer is shown in the top panel of Fig. 10. It is much broader and intense than the spectrum of HCN. The main reason is that the electronic transitions are allowed in HNC while for many of the lower electronic states they are forbidden for the HCN isomer, as manifested by the angular dependence of the transition dipole moment in Fig. 2. This result may have important implication for the relative abundances of each isomer in astrophysical environments illuminated by ultraviolet radiation as it predicts a faster destruction rate for HNC than for HCN.

E. Radiative lifetimes

In order to determine their radiative lifetimes, the Einstein coefficients of the adiabatic bound levels for the $4\,^1A'$, $2\,^1A''$,

and $3\,^1A''$ electronic states have been calculated according to Eq. (6). The first 120 bound levels on each of these 3 electronic states have been calculated and can be clearly assigned to either HCN or HNC, as shown in Fig. 9. According to Franck-Condon arguments, these states would decay towards levels on the same isomer. In fact, here we consider $J = 0 \rightarrow J' = 1$ transitions from the excited to the ground electronic states. The radiative lifetimes, $\tau = 1/A$, are shown in Fig. 11. For the $4\,^1A'$ and $2\,^1A''$ states, the lifetimes are clearly shorter for HNC than for HCN. This propensity rule is due to the value to the transition dipole moment, which is larger for $\gamma \approx 0$. In the $3\,^1A''$ state, the situation is reversed and the radiative lifetimes of HNC become longer. The cases out of scale in the $3\,^1A''$ correspond to those levels located in the middle well of Fig. 9 at $\gamma = 90°$ with very low Franck-Condon factors with the calculated bound rovibrational states on the X electronic state.

All the radiative lifetimes are longer than 10 ns, more than 4 orders of magnitude longer than the lifetimes associated to the peaks of the $1\,^1A''$ and $3\,^1A'$ states, which are shorter
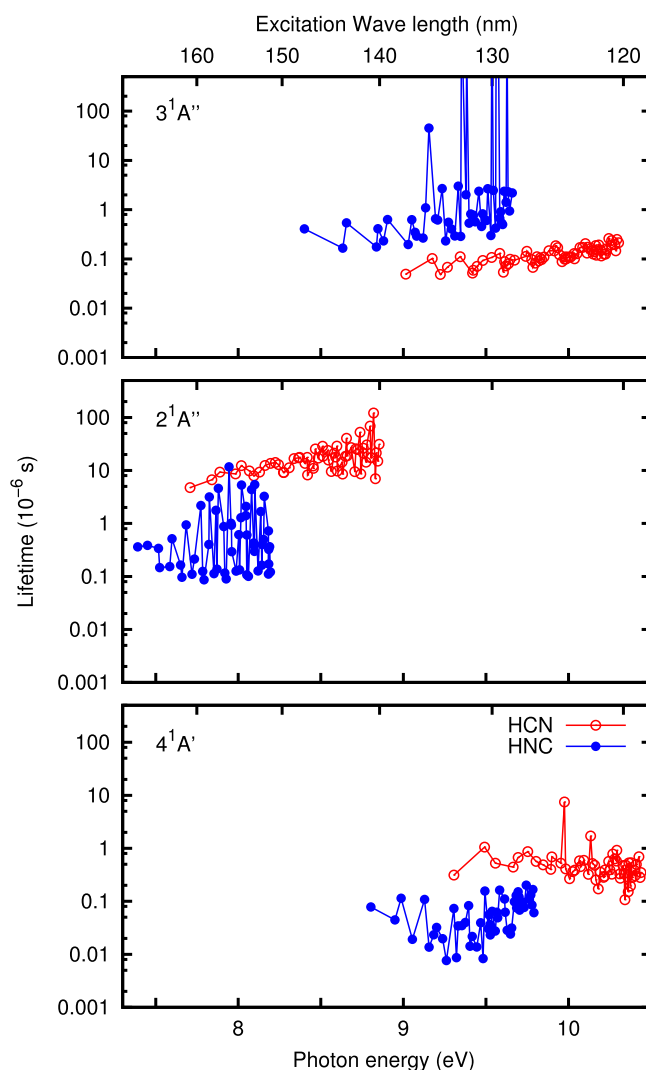

FIG. 11. Radiative lifetimes of the first 100 bound states of $4\,^1A'$ (bottom), $2\,^1A''$ (middle), and $3\,^1A''$ (top) electronic bound states. The two isomers have been distinguished as HCN for $\cos\gamma < 0$ or HNC for $\cos\gamma > 0$, according to Fig. 9.

than 1 ps. Assuming that the levels of the electronic bound state have similar (or shorter) dissociative lifetimes, the non-stimulated emission of photons seems to be rather inefficient. This is supported by measurements of branching ratios of excited CN ($A^2\Pi$) and CN ($B^2\Sigma^+$) through the detection of their emission to the ground CN ($X^2\Sigma^+$) state.[53] The quantum yield for CN ($B^2\Sigma^+$) emission accounts for about 30% at short wavelengths and $\approx$10% at longer wavelengths. For the CN ($A^2\Pi$) emission, the proportion is in the range of 40%-10% from high vibrational levels. Adding all of them, and considering the possible direct dissociation towards the ground CN($X^2\Sigma^+$), we can conclude that dissociation is the major channel and that emission is negligible.

V. CONCLUSIONS

The photoabsorption spectra of the HCN and HNC isomers have been studied for photon energies in the range 7-10 eV. For this purpose, the three-dimensional adiabatic PESs of the lowest 4 and 3 states of $^1A'$ and $^1A''$ symmetry, respectively, have been calculated. The transition electric dipole moments for transitions from the ground electronic state show drastic changes with the angle, reaching a value of zero at collinear HCN geometry for some excited electronic states due to symmetry. As a consequence, the $X^1A' \rightarrow 2^1A'$, $X^1A' \rightarrow 1^1A''$, and $X^1A' \rightarrow 2^1A''$ transitions are very weak from the HCN isomer, while they are quite intense from the HNC isomer.

The absorption toward the $2^1A'$, $3^1A'$, and $1^1A''$ valence states occurs through resonances supported by wells arising from avoided crossing with the excited electronic bound states. Most of these resonances dissociate through tunneling and have lifetimes that depend on the energy and nodal structure; some of them are estimated to be $\lesssim$1 ps. However, the resonances around the adiabatic dissociation threshold are extremely narrow, and they probably dissociate via electronic transitions. The resonances reached from HCN and HNC are different and have been identified as corresponding to different potential wells.

The electronic $4^1A'$, $2^1A''$, and $3^1A''$ states have deep wells for both HCN and HNC isomers, and the absorption adiabatic spectra are composed of discrete lines associated to bound-bound transitions. Their radiative lifetimes have been estimated to be in the range 0.01-100 ms, i.e., much longer than the dissociation lifetimes. Also the radiative transitions occur between states in either the HCN or the HNC isomer due to Franck-Condon factor arguments.

The total absorption cross section of HCN in the range 7-10 eV is in qualitative good agreement with the experimental one. One of the main differences is that the calculated resonances are too narrow compared with the experimental data because we have neglected electronic transitions in the present adiabatic approach.

The photoabsorption cross section of HNC is significantly higher than that of HCN in the 7-10 eV range, with important potential implications for the different photo-stability of the two isomers in astrophysical environments illuminated by ultraviolet radiation. Focusing on the 7-10 eV photon energy range and adopting the interstellar radiation field,[91]

the calculated cross sections imply that HNC would be photodissociated 5 times faster than HCN. This result could explain why HCN is more abundant than HNC in ultraviolet-illuminated interstellar regions. However, the relevant energy range of astrophysical interest extends up to an energy of 13.6 eV and experiments show that the photoabsorption cross section of HCN experiences a significant enhancement at photon energies above 10 eV.[55] Therefore, to assess the photodissociation rate of each isomer in ultraviolet-illuminated interstellar regions, it is necessary to extend the calculations of the photoabsorption cross section up to energies of 13.6 eV. Work in this direction is being conducted together with calculations of non-adiabatic transitions.

ACKNOWLEDGMENTS

[1]L. E. Snyder and D. Buhl, Astrophys. J. **163**, L47 (1971).
[2]M. Morris, B. Zuckerman, P. Palmer, and B. E. Turner, Astrophys. J. **170**, L109 (1971).
[3]A. M. Smith, S. L. Coy, and W. Klemperer, J. Mol. Spectrosc. **134**, 134 (1989).
[4]D. Jonas, X. Yang, and A. Wodtke, J. Chem. Phys. **97**, 2284 (1992).
[5]D. Romanini and K. K. Lehmann, J. Chem. Phys. **102**, 633 (1995).
[6]A. Maki, W. Quapp, S. Klee, G. Ch. Mellau, and S. Albert, J. Mol. Spectrosc. **180**, 323 (1996).
[7]A. Maki, G. Ch. Mellau, S. Klee, M. Winnewisser, and W. Quapp, J. Mol. Spectrosc. **202**, 67 (2000).
[8]G. Ch. Mellau, B. P. Winnewisser, and M. Winnewisser, J. Mol. Spectrosc. **249**, 23 (2008).
[9]G. Ch. Mellau, J. Mol. Spectrosc. **269**, 77 (2011).
[10]J. M. Bowman and B. Gadzy, J. Phys. Chem. A **101**, 6384 (1997).
[11]W. Jakubetz and B. L. Lan, Chem. Phys. **217**, 375 (1997).
[12]J. M. Bowman, S. Irle, K. Morokuma, and A. Wodtke, J. Chem. Phys. **114**, 7923 (2001).
[13]T. van Mourki, G. J. Harris, O. L. Polyansky, J. Tennyson, A. G. Csaszar, and P. J. Knowles, J. Chem. Phys. **115**, 3706 (2001).
[14]G. J. Harris, O. L. Polyansky, and J. Tennyson, Spectrochim. Acta, Part A **58**, 673 (2002).
[15]A. J. C. Varandas and S. P. J. Rodrigues, J. Phys. Chem. A **110**, 485 (2006).
[16]R. J. Barber, J. K. Strange, C. Hill, O. L. Polyansky, G. Ch. Mellau, S. N. Yurchenko, and J. Tennyson, Mon. Not. R. Astron. Soc. **437**, 1828 (2014).
[17]H. Liszt and R. Lucas, Astron. Astrophys. **370**, 576 (2001).
[18]B. E. Turner, L. Pirogov, and Y. C. Minh, Astrophys. J. **483**, 235 (1997).
[19]P. Pratap, J. E. Dickens, R. L. Snell, M. P. Miralles, E. A. Bergin, W. M. Irvine, and F. P. Schloerb, Astrophys. J. **486**, 862 (1997).
[20]T. Hirota, S. Yamamoto, H. Mikami, and M. Ohishi, Astrophys. J. **503**, 717 (1998).
[21]P. Hily-Blant, M. Walmsley, G. Pineau des Forêts, and D. Flower, Astron. Astrophys. **512**, A41 (2010).
[22]P. Schilke, C. M. Walmsley, G. Pineau des Forêts, E. Roueff, D. R. Flower, and S. Guilloteau, Astron. Astrophys. **256**, 595 (1992).
[23]D. Graninger, E. Herbst, K. Öberg, and A. I. Vasyunin, Astrophys. J. **787**, 745 (2014).
[24]M. Jin, J.-E. Lee, and K.-T. Kim, Astrophys. J., Suppl. Ser. **219**, 2 (2015).
[25]D. Graninger, K. Öberg, C. Qi, and J. Kastner, Astrophys. J., Lett. **807**, L15 (2015).
[26]V. Bujarrabal, A. Fuente, and A. Omont, Astron. Astrophys. **285**, 247 (1994).

[27]J. Cernicharo, F. Daniel, A. Castro-Carrizo, M. Agundez, N. Marcelino, C. Joblin, J. R. Goicoechea, and M. Guélin, Astrophys. J., Lett. **778**, L25 (2013).

[28]N. Harada, D. Riquelme, S. Viti, I. Jiménez-Serra, M. A. Requena-Torres, K. M. Menten, S. Martín, R. Aladro, J. Martin-Pintado, and S. Hochgürtel, Astron. Astrophys. **584**, A102 (2015).

[29]Y. Gao and P. M. Solomon, Astrophys. J., Suppl. Ser. **152**, 63 (2004).

[30]M. Guélin, P. Salomé, R. Neri *et al.*, Astron. Astrophys. **462**, L45 (2007).

[31]S. Aalto, S. García-Burillo, S. Müller *et al.*, Astron. Astrophys. **537**, A44 (2012).

[32]D. D. Lis, D. Bockelée-Morvan, J. Boissier, J. Crovisier, N. Biver, and S. B. Charnley, Astrophys. J. **675**, 931 (2008).

[33]R. Moreno, E. Lellouch, L. M. Lara *et al.*, Astron. Astrophys. **536**, L12 (2011).

[34]E. Sarrasin, D. Ben Abdallah, M. Wernli, A. A. Faure, J. Cernicharo, and F. Lique, Mon. Not. R. Astron. Soc. **404**, 518 (2010).

[35]M. R. Hogerheijde, D. J. Jansen, and E. F. van Dishoeck, Astron. Astrophys. **294**, 792 (1995).

[36]S. Cuadrado, private communication (2016); see also S. Cuadrado, J. R. Goicoechea, P. Pilleri, J. Cernicharo, A. Fuente, and C. Joblin, Astron. Astrophys. **575**, A82 (2015).

[37]J.-C. Loison, V. Wakelam, and K. M. Hickson, Mon. Not. R. Astron. Soc. **443**, 398 (2014).

[38]F. Dumouchel, J. Klos, and F. Lique, Phys. Chem. Chem. Phys. **13**, 8204 (2011).

[39]D. Ben Abdallah, F. Najar, N. Jaidane, F. Dumouchel, and F. Lique, Mon. Not. R. Astron. Soc. **419**, 2441 (2012).

[40]G. Herzberg and K. K. Hines, Can. J. Phys. **35**, 842 (1957).

[41]Y. C. Hsu, M. A. Smith, and S. C. Wallace, Chem. Phys. Lett. **111**, 219 (1984).

[42]A. Meenakshi and K. K. Innes, J. Chem. Phys. **84**, 6550 (1986).

[43]R. Eng, T. Carrington, C. H. Dugan, S. V. Filseth, and C. M. Sadowski, Chem. Phys. **113**, 119 (1987).

[44]D. M. Jonas, X. Zhao, K. Yamanouchi, P. G. Green, G. W. Adamson, and R. W. Field, J. Chem. Phys. **92**, 3988 (1990).

[45]M. Peric, J. Buenker, and S. D. Peyerimhoff, Mol. Phys. **64**, 8433 (1988).

[46]D. Xu, D. Xie, and H. Guo, Chem. Phys. Lett. **345**, 517 (2001).

[47]D. Xu, D. Xie, and H. Guo, J. Phys. Chem. A **106**, 10174 (2002).

[48]D. Xu, D. Xie, and H. Guo, J. Chem. Phys. **116**, 10626 (2002).

[49]D. Xu, H. Guo, and D. Xie, J. Theor. Comput. Chem. **2**, 639 (2003).

[50]M. T. Mcpherson and J. P. Simons, J. Chem. Soc., Faraday Trans. 2 **74**, 1965 (1978).

[51]D. T. Chuljian, J. Ozment, and J. Simons, J. Chem. Phys. **89**, 176 (1984).

[52]M. Peric, J. Buenker, and S. D. Peyerimhoff, Mol. Phys. **62**, 1323 (1987).

[53]L. C. Lee, J. Chem. Phys. **72**, 6414 (1980).

[54]T. Nagata, T. Kondow, Y. Ozaki, and K. Kuchitsu, Chem. Phys. **57**, 45 (1981).

[55]J. A. Nuth and S. Glicker, J. Quant. Spectrosc. Radiat. Transfer **28**, 223 (1982).

[56]T. Shiozaki, G. Knizia, and H-J. Werner, J. Chem. Phys. **134**, 034113 (2011).

[57]MOLPRO is a package of *ab initio* programs designed by H.-J. Werner and P. J. Knowles and with contributions from, J. Almlöf, R. D. Amos, A. Berning, M. J. O. Deegan, F. Eckert, S. T. Elbert, C. Hampel, R. Lindh, W. Meyer, A. Nicklass, K. Peterson, R. Pitzer, A. J. Stone, P. R. Taylor, M. E. Mura, P. Pulay, M. Schütz, H. Stoll, T. Thorsteinsson, and D. L. Cooper (version 2012).

[58]T. Shiozaki and H.-J. Werner, J. Chem. Phys. **134**, 184104 (2011).

[59]K. A. Peterson and H.-J. Werner, J. Chem. Phys. **128**, 084102 (2008).

[60]C. de Boor, *A Practical Guide to Splines* (Springer-Verlag, New York, 1978).

[61]R. F. Boisvert, GAMS, the program was downloaded from 2015.

[62]N. Sathyamurthy and L. M. Raff, J. Chem. Phys. **63**, 464 (1975).

[63]G. M. Schwenzer, S. V. O'Neil, H. F. Schaefer III, C. P. Baskin, and C. F. Bender, J. Chem. Phys. **60**, 2787 (1974).

[64]G. M. Schwenzer, H. F. Schaefer III, and C. F. Bender, J. Chem. Phys. **63**, 569 (1974).

[65]M. Peric, H. Dohmann, and S. D. Peyerimhoff, Z. Phys. D **5**, 65 (1987).

[66]M. K. Nayak, R. K. Chaudhuri, and S. N. L. G. Krishnamachari, J. Chem. Phys. **122**, 184323 (2005).

[67]G. Herzberg, *Electronic Spectra and Electronic Structure of Polyatomic Molecules* (van Nostrand Reinhold Company, New York, 1966).

[68]R. N. Zare, *Angular Momentum* (John Wiley and Sons, Inc., 1988).

[69]T. González-Lezana, A. Aguado, M. Paniagua, and O. Roncero, J. Chem. Phys. **123**, 194309 (2005).

[70]A. Zanchet, O. Roncero, T. González-Lezana, A. Rodríguez-López, A. Aguado, C. Sanz-Sanz, and S. Gómez-Carrasco, J. Phys. Chem. A **113**, 14488 (2009).

[71]M. Paniagua, A. Aguado, M. Lara, and O. Roncero, J. Chem. Phys. **111**, 6712 (1999).

[72]A. Aguado, M. Paniagua, C. Sanz-Sanz, and O. Roncero, J. Chem. Phys. **119**, 10088 (2003).

[73]S. Gómez-Carrasco, A. Aguado, M. Paniagua, and O. Roncero, J. Chem. Phys. **125**, 164321 (2006).

[74]C. Lanczos, J. Res. Natl. Bur. Stand. **45**, 255 (1950).

[75]J. K. Cullum and R. A. Willoughby, *Lanczos Algorithms for Large Symmetric Eigenvalues Computations* (Birkhäuser, Boston, 1985).

[76]C.-E. Fröberg, *Numerical Mathematics: Theory and Computer Applications* (The Benjamin/Cummings Publishing Company, 1985).

[77]R. E. Wyatt, Adv. Chem. Phys. **LXXIII**, 231 (1989).

[78]O. Roncero, D. Caloto, K. C. Janda, and N. Halberstadt, J. Chem. Phys. **107**, 1406 (1997).

[79]Y. Huang, D. J. Kouri, and D. K. Hoffman, J. Chem. Phys. **101**, 10493 (1994).

[80]V. A. Mandelshtam and H. S. Taylor, J. Chem. Phys. **103**, 2903 (1995).

[81]Y. Huang, S. S. Iyengar, D. J. Kouri, and D. K. Hoffman, J. Chem. Phys. **105**, 927 (1996).

[82]G. J. Kroes and D. Neuhauser, J. Chem. Phys. **105**, 8690 (1996).

[83]R. Chen and H. Guo, J. Chem. Phys. **105**, 3569 (1996).

[84]S. K. Gray and G. G. Balint-Kurti, J. Chem. Phys. **108**, 950 (1998).

[85]R. Sadeghi and R. T. Skodje, J. Chem. Phys. **102**, 193 (1995).

[86]C. L. Russell and D. E. Manolopoulos, Chem. Phys. Lett. **256**, 465 (1996).

[87]N. Bulut, J. Klos, and O. Roncero, J. Chem. Phys. **142**, 214310 (2015).

[88]J. Bowman, B. Gadzy, J. Bentley, T. J. Lee, and C. E. Dateo, J. Phys. Chem. **99**, 308 (1993).

[89]A. J. C. Varandas and S. P. J. Rodrigues, J. Chem. Phys. **106**, 9647 (1997).

[90]D. Lauvergnat, A. Simon, and P. Maitre, Chem. Phys. Lett. **350**, 345 (2001).

[91]B. T. Draine, Astrophys. J., Suppl. Ser. **36**, 595 (1978).